Geophysical Journal International

Geophys. J. Int. (2025) **243,** 1–14
Advance Access publication 2025 August 29
Research Paper

https://doi.org/10.1093/gji/ggaf344

A method for the prediction of seismic discontinuity topography from thermochemical mantle circulation models

Gwynfor T. Morgan ,[1] J. Huw Davies,[1] Robert Myhill ,[2] James Wookey[2] and James Panton[1,*]

[1] *School of Earth and Environmental Sciences, Cardiff University, Park Place, Cardiff, CF10 3AT, UK. E-mail: morgangt2@cardiff.ac.uk*
[2] *School of Earth Sciences, University of Bristol, Queens Road, Bristol, BS8 1RJ, UK*

Accepted 2025 August 28. Received 2025 August 18; in original form 2025 June 11

SUMMARY

We demonstrate a method for the prediction of seismic discontinuity topography from thermochemical Mantle Circulation Models (MCMs). We find the discontinuity depth by using the peak reflectivity at each location in our mantle transition zone, taking account of compositional as well as thermal variations. We make some comparisons of our predicted topographies with those observed using SS-precursors, developing a simple smoothing filter to capture the distribution of sensitivity of a published topography model—finding that such filtering has a significant impact on the predicted discontinuity topographies. We also consider the significance of lateral variations in reflectivity or reflection amplitude in our predicted data sets and the real Earth. Finally, we consider what aspects of mantle-transition zone discontinuity structure would be matched by the predicted discontinuity structure from an Earth-like MCM—particularly the mean depths of the discontinuities, the amplitude of the topography and the shape of its spherical harmonic spectra.

Key words: Phase transitions; Mantle; Seismic discontinuities.

1 INTRODUCTION

Discontinuities in the material properties of the Earth's mantle are a long-standing feature of 1-D seismological models (e.g. Jeffreys & Bullen 1940) and for over 75 years have been associated with phase transitions (e.g. Birch 1952), where the stable material phase changes due to increasing pressure. In the mantle transition zone the principal discontinuities around 410 and 660 km depth (hereafter referred to as 'd410' and 'd660') are usually associated with the reactions Ol (Olivine) $\rightarrow$ Wd (Wadsleyite) (e.g. Ringwood & Major 1970) and Rw (Ringwoodite) $\rightarrow$ Brm (Bridgmanite) + Pc (Periclase) (e.g. Ito *et al.* 1984). As these are chemical reactions, variations in the depth of the phase transition due to temperature variations in a convecting mantle (potentially impacting the regime of the convection, e.g. Christensen & Yuen 1985) have been expected for a long time, as was the possibility of their seismic observation by Verhoogen (1965).

Topography on d410 and d660 was first recognized in the early 1990s (e.g. Revenaugh & Jordan 1991; Shearer & Masters 1992), using ScS reverberations and SdS underside reflections (SS precursors). Since then, many global studies have been published, principally using SS precursors (e.g. Flanagan & Shearer 1998; Gu *et al.* 1998, 2003; Houser *et al.* 2008; Lawrence & Shearer 2008; Houser & Williams 2010; Houser 2016; Yu *et al.* 2017; Huang *et al.* 2019; Guo & Zhou 2020; Waszek *et al.* 2021b) as well as a larger number of contributions using receiver function methods in regions with a high density of seismic stations (e.g. Chevrot *et al.* 1999; Collier & Helffrich 2001; Thompson *et al.* 2011; Lee *et al.* 2014; Cottaar & Deuss 2016; Maguire *et al.* 2018; Keifer & Dueker 2019; Rao *et al.* 2020; Yu *et al.* 2020; Agius *et al.* 2021; Burky *et al.* 2023; Liu *et al.* 2023; Bonatto *et al.* 2024; Glasgow *et al.* 2024).

Global studies largely find peak-to-peak topography amplitude on the order of $\sim$ 40km on both discontinuities, and a strong positive correlation between the observed depths of d410 and d660 (e.g. Houser & Williams 2010). This last observation runs counter to the expected anticorrelation from the opposing Clapeyron slopes of the olivine-out and ringwoodite-out reactions. It is important to recognize that a correlation in mapped topography does not necessarily imply a true correlation in the physical topography of the 410 and 660 km discontinuities. A discrepancy may arise for several reasons: (a) SS-precursor resolution is limited and differs between the 410 and 660, (b) global coverage of SS-precursors is incomplete and (c) the conversion from differential arrival times to discontinuity depths relies on simplifying assumptions, such as mantle homogeneity and locally flat, sharp discontinuities.

Even if the correlation in mapped topography does reflect a genuine correlation, the underlying cause remains uncertain. There is currently no consensus among the seismological, mineral physics

---

[*] Now at: Institut für Geophysik und Meteorologie, Universität zu Köln, Albertus-Magnus-Platz, D-50923, Köln, Deutschland.

or geodynamics communities regarding the dominant mechanism driving such a correlation. Explanations have included (i) The 3-D nature of mantle thermal structure (e.g. Shearer & Masters 1992; Goes *et al.* 2022), (ii) compositional variations (e.g. Houser *et al.* 2008) and (iii) a positive Clapeyron slope at high temperatures controlling d600 (e.g. Houser & Williams 2010; Waszek *et al.* 2021b) have all been suggested. Whilst the mid-mantle is likely to be a region with strong variations in water content, and regions with high water content are expected to favour the stability of wadsleyite and ringwoodite as these phases hold more water than those shallower or deeper in the mantle (e.g. Ohtani 2021), it is considered unlikely that this will result in a positive correlation of d410 and d660 (Houser 2016; Muir *et al.* 2021).

SdS topographies are typically corrected for mantle structure (using 3-D seismic velocity tomography models) and crustal structure (which might advance or delay the SS phase compared to a global average, meaning that a discontinuity is interpreted as shallower or deeper than it is actually) using the model CRUST 1.0 or its predecessors (Laske *et al.* 2012); however the lithosphere also has an extremely heterogeneous structure (e.g. Pasyanos *et al.* 2014) which is not usually corrected for—this could also explain the positive d410-d660 correlation (e.g. Tauzin *et al.* 2022).

As the topographies of d410 and d660 are recognized as being dominantly controlled by temperature, there is a long-standing understanding that it should be possible to invert the depths of the discontinuities and their topography for the average and range of temperatures in the mantle transition zone. Shearer & Masters (1992) estimated a temperature range at 660 km depth of between 300 and 600 K based on a simple calculation from their observed topography and contemporary estimates of the Clapeyron slope of the post-spinel reaction. However, subsequent workers (e.g. Deuss *et al.* 2006) showed that the d660 could not be understood simply using the post-spinel reaction—and that other reactions and potentially compositional variations were important in controlling the depth of the seismic discontinuity. Ritsema *et al.* (2009) used the differential traveltimes of S410S and S660S phases (i.e. a proxy for MTZ thickness) to constrain the mantle potential temperature in the North Pacific (1650 ± 100 K). Waszek *et al.* (2021b) inverted SdS data separately for 410 and 660 topographies and then used the calculated MTZ thicknesses to invert for an average potential temperature of 1630 K with 'peak-to-peak variations' of $\sim$ 350K. All of these inversions assume a single global mineral physics model—usually a mechanically mixed (MM) pyrolite model with $f_{\text{bas}} \sim 0.2$. The effect of lateral composition variations has only recently been considered. Tauzin *et al.* (2022) inverted reflection amplitude and transition zone thickness for composition as well as potential temperature, finding that the basalt fraction (f_{bas}) varied from 0.0 to 0.8 in the mid mantle, finding a similar mantle potential temperature to Waszek *et al.* (2021b) but a slightly higher temperature range of $\sim$ 450 K. However, because seismic waves have limited resolution, the range of discontinuity depths estimated from seismic observations will be an underestimate. Therefore, the range of temperatures will also be underestimated.

The MTZ is dynamically complex—and discontinuity topographies could represent a useful constraint on geodynamic models in the mantle transition zone. Papanagnou *et al.* (2023) outlined a method for predicting seismic discontinuity topography using the thermal structure of a geodynamic model, and examined the effect of using diverse mineral physics tables on the predicted topographies—which had a large effect when applied globally. Many geodynamic codes are now able to produce thermochemical outputs [e.g. TERRA (Baumgardner 1983; Bunge & Baumgardner 1995; Stegman 2003), ASPECT (Kronbichler *et al.* 2012; Heister *et al.* 2017), stag3D (Tackley 1993; Tackley & Xie 2002)]—including those generated by geological processes (such as melting; e.g. Van Heck *et al.* 2016) and then dispersed through the silicate Earth over Earth history. Recent work (Yan *et al.* 2020) suggests that the mantle transition zone could host significant compositional heterogeneity.

Here we present a new method for predicting discontinuity topography in thermochemical mantle circulation models. Further, a comparison to global observations with a seismologically motivated filter for the sensitivity of the SS precursors is illustrated. We use a MCM previously introduced to the literature by Davies *et al.* (2025) to illustrate the minor effect of different mixing models and the more significant effect of the filtering applied, and demonstrate how a single MCM is evaluated against a published topography model.

2 METHODS

2.1 Geodynamic model

We demonstrate our method using a single mantle circulation model 'm_cc_066_u'—detailed at length in Davies *et al.* (2025). This model was run in TERRA (Baumgardner 1983), which solves the Stokes equations on an iscosahedral grid refined to give a grid spacing of $\sim$ 45km in the mid-mantle. Model parameters are summarized in Table 1. At this resolution we are not able to resolve upper mantle viscosities strictly compatible with the Haskell constraint of 1×10^{21} Pa s, but instead use a slightly higher reference viscosity of 4×10^{21} Pa s, which will result in slightly stronger thermal anomalies that are broader than in the real Earth. The upper boundary is driven using the plate motion model of Müller *et al.* (2022). Radial average viscosity structure is illustrated in Fig. S1. 'm_cc_066_u' was run using a cooling core–mantle boundary (CMB) thermal boundary condition (Davies 2015), and is internally heated according to concentration of heat producing elements distributed on particles (see below) in the simulated mantle (Panton *et al.* 2022), and is compressible with a Murnaghan equation of state (Bunge *et al.* 1997). The radial viscosity structure features a $\sim$ 100 km thick lithosphere that is 100× more viscous than the upper mantle, allowing thermal conduction to dominate there. A comparison to seismic observables sensitive the detail of the thermochemical structure in the MTZ is then motivated both to demonstrate this method and to evaluate a MCM with reasonable parameters. The thermochemical structure at 410 and 660 km depth in simulation m_cc_066_u is illustrated in Fig. S2.

2.1.1 Composition in TERRA

For full details of the implementation of particles and melting in TERRA, the reader is referred to Stegman (2003), Van Heck *et al.* (2016) and Panton *et al.* (2022). TERRA advects particles through its simulations according to the flow calculated on the regular icosohedral grid nodes. These particles can be used as passive tracers, but here have an active effect on the flow due to density anomalies dependent on their bulk composition. In m_cc_066_u, basalt is 5 per cent less dense than lherzolite between 660 and 740 km depth. This results in a slight 'basalt density filter' effect where basaltic material is more buoyant than pyrolitic material in the lower mantle transition zone, but the resulting radial basalt segregation is not as extreme as that advocated for by Yan *et al.* (2020) or that Tauzin *et al.* (2022) suggest by inversion of global SS precursor structure. Elsewhere, basalt is denser than pyrolite or harzburgite.

Table 1. Parameters used in mantle circulation model ‘m_cc_066_u’

Symbol	Parameter	Value	
k	Thermal conductivity	$4\ \mathrm{Wm}^{-1}\ \mathrm{K}^{-1}$	a
C_P	Specific heat capacity	$1100\ \mathrm{J\,kg}^{-1}\ \mathrm{K}^{-1}$	b
T_{Surf}	Surface temperature	300 K	–
T_{CMB}	CMB Temperature (average over run)	4007 K	c
γ_{410}	$\frac{\mathrm{d}P}{\mathrm{d}T}$ of $Ol \rightarrow Wd$	$+1.5\ \mathrm{MPa\,K}^{-1}$	–
γ_{660}	$\frac{\mathrm{d}P}{\mathrm{d}T}$ of $Rw \rightarrow Brm + Pc$	$-1\ \mathrm{MPa\,K}^{-1}$	–
η_0	Reference viscosity	4×10^{21} Pa s	–
E_A	Activation Energy	1.75	
B	Basalt buoyancy number	0.66	
$\frac{\Delta\rho_{410}}{\rho_{410}}$	$Ol \rightarrow Wd$ density change	6.37 %	
$\frac{\Delta\rho_{660}}{\rho_{660}}$	$Rw \rightarrow Brm + Pc$ density change	9.08 %	

Initial Condition: The mantle circulation model is initialized from a mantle convection model run for 2 Gyr. The mantle is preconditioned for 200 Myr using the first stage of the plate model.

[a] (p. 122, Clauser & Huenges 1995)

[b] (Panton 2020)

[c] cooling CMB condition, see main text.

Table 2. Assumed molar composition for our three characteristic lithologies; harzburgite, lherzolite and basalt.

	Harzburgite (Hzb)	**Lherzolite** (Lhz)	**Basalt** (Bas)
SiO_2	36.184	38.819	52.298
MgO	56.559	49.894	15.812
FeO	5.954	6.145	7.121
CaO	0.889	2.874	13.027
Al_2O_3	0.492	1.963	9.489
Na_2O	0.001	0.367	2.244

Bulk composition is described using a parameter (C) that varies between 0 and 1 describing the relative depletion or enrichment of the particle—a C-value of 0 represents entirely depleted material [i.e. Harzburgite (Hzb)], of 0.2 represents bulk mantle material [i.e. Lherzolite (Lhz)] and of 1 represents entirely enriched material [i.e. Basalt (Bas)/Pyroxenite]. Particles are initialized with an even distribution throughout the whole mantle with half of all particles being lherzolitic, 40 per cent harzburgitic and 10 per cent basaltic—resulting in an initial average C-Value of 0.2. The particles are then advected through the simulation, following the whole-mantle circulation. If the pressure–temperature conditions of the particle put it over the solidus in the shallow mantle, it undergoes partial melting—melt is extracted towards the surface resulting in particles near the surface becoming enriched (basaltic) while the melt source particle becomes depleted (harzburgitic). As well as bulk composition, various geochemical parameters (e.g. Panton *et al.* 2022) including abundances of heat producing elements evolving with melt and radioactive decay are recorded on the particles but are not of interest here.

2.2 Mineral physics models

In order to predict the discontinuity topography, we require look-up tables of density (ρ), P-wave velocity (V_P) and S-wave velocity (V_S) in pressure–temperature space for each of our assumed end-member compositions. The tables used by Davies *et al.* (2025) are used here as well. We describe our end member lithologies by using six oxide components (see Table 2)—chosen to fit published data sets for Harzburgite, Lherzolite and Basalt (Baker & Beckett 1999; Walter 2003; White & Klein 2014, respectively).

Equilibrium mineral assemblages (with resultant elastic and thermodynamic properties) are calculated by Gibbs free energy minimization using Perple_X (Connolly 2009), with thermodynamic data from Stixrude & Lithgow-Bertelloni (2005, 2011, 2022). The isotropic elastic seismic velocities are corrected for anelasticity using the model ‘Q7g’ (Goes *et al.* 2004; Maguire *et al.* 2016). The V_S structure of the lherzolite, harzburgite basalt and pyrolitic assemblage (MM18) are shown in Fig. S3.

2.3 Prediction of seismic velocity discontinuity (‘local mechanical mixing and reflectivity’)

Whilst composition is tracked on the fine scale length of the particles, the total proportion of harzburgite, lherzolite and basalt in the region surrounding each node is also recorded. This then allows us to predict the thermochemical discontinuity topography on the regular TERRA grid at a spacing of $\sim$ 45km laterally in the mid-mantle, far finer than the thermochemical structure that SS precursors are sensitive to given that the lateral extent of the first Fresnel zone of S660S and S410S are both $\sim$ 1000 km (Guo & Zhou 2020), and the full Fresnel zones have sensitivity that extend for several times as far dependent on the azimuth to the source–receiver pair and bands of positive- and negative-sensitivity extending away from the ray-theoretical bounce-point.

Vertically, however, a 45 km vertical resolution is far too coarse to resolve the phase transition, so we first interpolate the data from the coarse TERRA grid onto a finer vertical grid centred on a target depth (for this work 410 and 660 km) for each horizontal position (see Fig. 1a). The thermal field of our geodynamic model is smooth, so we interpolate temperature linearly (similar to the method used by Papanagnou *et al.* 2023) between the TERRA grid-points and since chemical diffusion is very slow composition is interpolated by a nearest neighbour scheme. This allows us to integrate the chemical heterogeneity from the MCM into our discontinuity prediction. Given recent geodynamic and seismologic work (e.g. Yan *et al.* 2020; Goes *et al.* 2022; Tauzin *et al.* 2022) chemical heterogeneity is expected to be quite high in the Earth’s mantle, and particularly in the mantle transition zone.

A mechanical mixing calculation is performed between the tracked compositions at each point to evaluate ρ, V_S and V_P on this refined grid (Fig. 1b). To gain a representative estimate of the

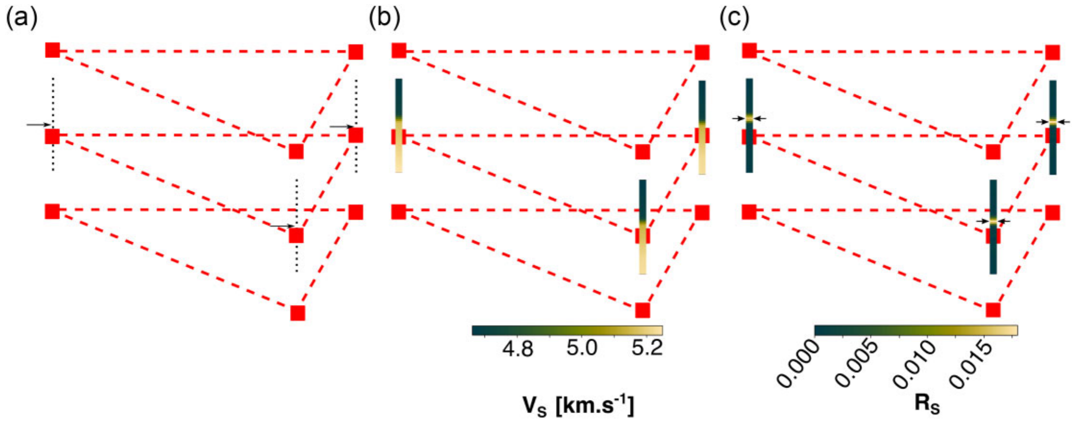

Figure 1. Sketch of method introduced here. (a) The gridding used for the geodynamic modelling is too coarse for the purposes of finding the discontinuity structure, so the thermal and chemical structures are interpolated onto a finer grid centred on a reference depth (i.e. 410 or 660 km). (b) temperature, pressure and composition at each interpolated location is used to compute V_S, V_P and ρ. (c) These are then used to compute *S*-wave reflectivity R_S at each interpolated location, and the highest reflectivity is used as the discontinuity depth at that location.

bulk properties, a harmonic average is used for densities and velocities

$$\frac{1}{\Psi^{P,T}_{\mathrm{Bulk}}} = \frac{f_{\mathrm{Lhz}}}{\Psi^{P,T}_{\mathrm{Lhz}}} + \frac{f_{\mathrm{Hzb}}}{\Psi^{P,T}_{\mathrm{Hzb}}} + \frac{f_{\mathrm{bas}}}{\Psi^{P,T}_{\mathrm{bas}}}, \tag{1}$$

where $\Psi^{P,T}_{m}$ represents either the density or one of the seismic velocities of the material (m) at the relevant pressure (P) and temperature (T). We refer to this calculation, where the fraction of each end-member in the averaging scheme varies according to the local abundance of each end-member, as 'local mechanical mixing' to differentiate it from the assumption of a uniform mechanical mixture globally.

Having produced the high-resolution density and velocity profiles at each node, we predict the topography as observed by SS precursors, assuming vertical incidence. First, the vertical reflectivity is calculated for each depth i as the impedance contrast across that depth,

$$R^i_S = \frac{(\rho^{i+1}+\rho^i)(V^{i+1}_S+V^i_S)-(\rho^{i-1}+\rho^i)(V^{i-1}_S+V^i_S)}{(\rho^{i+1}+\rho^i)(V^{i+1}_S+V^i_S)+(\rho^{i-1}+\rho^i)(V^{i-1}_S+V^i_S)}. \tag{2}$$

To then find the discontinuity depth, the peak vertical reflectivity is found at each lateral node, and the corresponding depth used (Fig. 1c) since we assume the peak vertical reflectivity is associated with the depth of the discontinuity. The peak vertical reflectivity represents an upper bound for the actual reflectivity for the offsets used in SS precursor studies since the SS-precursor phase is not strictly vertically incident on the discontinuity. Whilst for 410, this is usually unambiguous as across compositions it is generally controlled by the Ol-out reaction (until the pyroxene-garnet reaction dominates at high basalt fraction), the region around 660 is much more complex. At cool temperatures the spinel-out reaction is accomplished via akimotoite (e.g. Yu *et al.* 2011; Cottaar & Deuss 2016) and at high basalt fraction the spinel out reaction is replaced by the deeper garnet-out reaction (e.g. Jenkins *et al.* 2016)—together these can result in multiple peaks and broad regions of elevated reflectivity (see Fig. S4). For simplicity we pick the depth of maximum reflectivity.

2.4 The 'bounce-point-spherical cap filter'—a simple filter for SS precursors

Later, we will compare these predicted topographies to those observed using SS-precursors, and here describe a simple filter to permit a meaningful comparison.

As the distribution of sources, receivers and therefore bounce-points, are highly non-uniform and SS-precursor sensitivity extends away from the ray-theoretical bounce-point (e.g. Neele *et al.* 1997; Dahlen 2005; Guo & Zhou 2020) we implement here a first-order approximation of the sensitivity of the precursors to mantle transition zone seismic structure distributed with the ray-theoretical bounce-points. We approximate the sensitivity of the precursor (typically of period ∼ 20 s), which is actually a complex region of positive and negative traveltime sensitivity, as a spherical cap of radius 500 km. This spherical cap represents a multi-azimuthal average of *SS-SdS* traveltime sensitivity and is similar in size to the first Fresnel zone of the SS precursor (e.g. Dahlen 2005). Similar caps are typically used in stacking these SS precursor data (e.g. Houser *et al.* 2008; Guo & Zhou 2020). As well as this finite-far-field sensitivity seismic waves cannot resolve infinitely thin radial seismic impedance structures. Usually it is assumed that impedance contrasts less than a quarter wavelength thick cannot be resolved (e.g. Chambers *et al.* 2005). Using array processing does allow a smaller effective Fresnel zone to be formed (e.g. Rost & Thomas 2009) between a seismic source and an array of receivers, but due to the additional labour required for the array processing, coverage is at present much more limited than for more conventional SS-precursor studies (e.g. Saki *et al.* 2024), although it allows the consideration of important effects, such as out-of-plane energy, yielding a more accurate assessment of reflector depths (e.g Rochira & Thomas 2023).

This 'filter' is very simple and does not capture all of the complexities of the physics of seismic ray reflection. In regions with many bounce-points and a reasonable spread of azimuths (e.g. the North Pacific) use of the true sensitivity kernels is unlikely to have a significant impact on the expected topography. However, in poorly constrained regions we likely underpredict the high spherical harmonic degree structure compared to that retrieved by a realistic kernel. We also do not consider the effect of earthquake focal mechanisms (which would create a null-sensitivity along the nodal planes; Zhao & Chevrot 2003) or anisotropic velocities in the mid-upper mantle (Huang *et al.* 2019) since we judge these to have

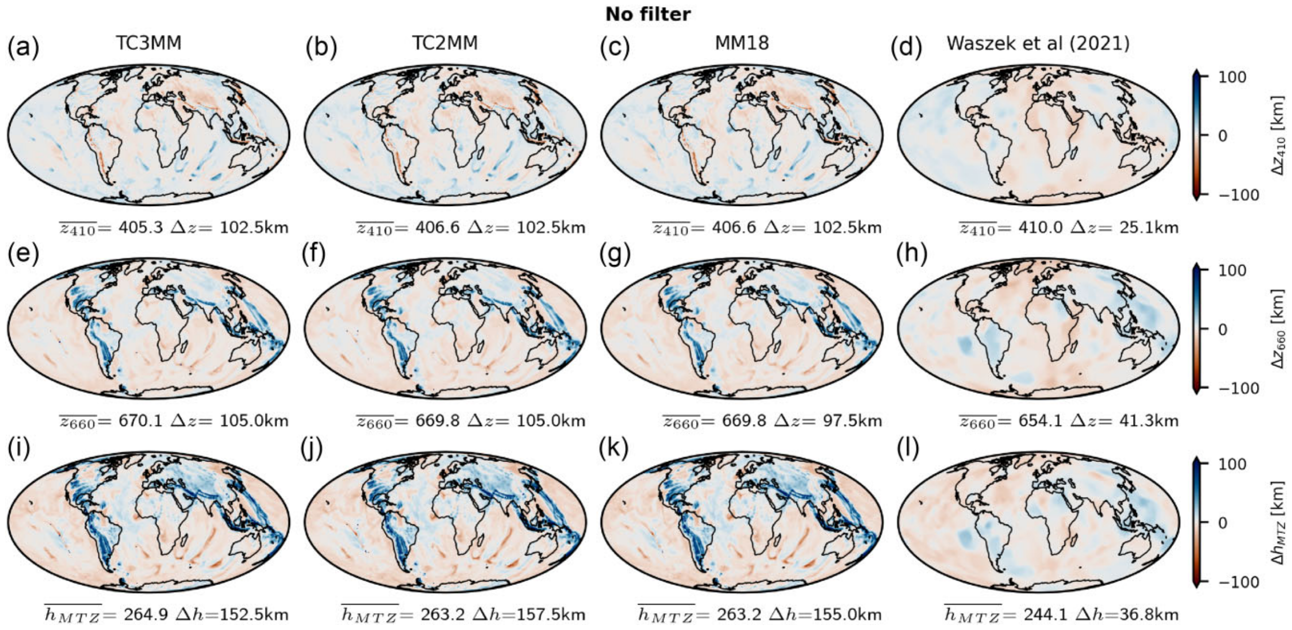

Figure 2. Topography on 410 (a–d) and 660 (e–h) discontinuities and MTZ thickness variations (i–l) calculated by method described here for model 'm_cc_066_u' compared to the topography found for the Earth by Waszek *et al.* (2021b) in the righthand most column (d, h, l). The other columns denote different methods of mechanical mixture. *'TC3MM'*: topography predicted by three end-member local mechanical mixing calculation using a equilibrium assemblage table for Lhz. *'TC2MM'*: topography predicted by two end-member local mechanical mixing calculation using a Mechanical Mixture table of 80 per cent Hzb, 20 per cent Bas for Lhz. *'MM18'*: topography predicted by a global mechanical mixing calculation of 18 per cent Bas and 82 per cent Hzb.

a secondary impact on recovered topographies compared to the above.

To produce the filtered topographies, we do the same upscaling and local mechanical mixing procedure described above, but instead of focusing on the region around the discontinuities, we predict the fine-scale material property structure on the length scale of the thermodynamic tables (2.5 km) radially throughout the MTZ. For a 20s period SS precursor just beneath d660, a quarter wavelength is 30 km, so we use a rolling window 30 km thick to find the radial reflectivity structure through the whole MTZ at each lateral point. We then pick the depths with the brightest reflection around 410 km $(200 - 480\,\text{km})$ and 660 km $(600 - 850\,\text{km}$ depth) depth as the depths of the discontinuities. To filter the predicted topographies for the lateral sensitivity of the SS precursor, we take a simple average of the discontinuity depth within a radius of 500 km of the bounce-points for the source–receiver pairs used by Waszek *et al.* (2021b).

These are then compared directly to the Waszek *et al.* (2021b) topography model. In this study we approximate the spatial averaging of the SS-precursor performed by Waszek *et al.*, as exact reproduction would require original data from the study. We expect the exact choice of spatial averaging to have a negligible impact on our results.

3 RESULTS

3.1 Local mechanical mixing with three end members: TC3MM

First we consider the topographies calculated with three end members, referring to this local mechanical mixing model as 'TC3MM' (since this takes account of the full thermochemical structure with three-end members). The global discontinuity topography predicted by this method is illustrated in Figs 2(a), (e) and (i). The topography on these reactions is dominated by the focused upwellings (approximating plumes) and downwellings (approximating slabs) that pass through the MTZ of the model—but there are other regions of complex topography particularly on d410 above flat-lying slabs such as beneath Eastern Canada and NE Brazil. On d410, as suggested by the classic understanding that the discontinuity is controlled by the olivine-out reaction with a positive Clapeyron slope, hot upwellings are associated with a deepening of the discontinuity and cool downwellings are associated with an elevation.

On d660, the broad-scale structure follows the trends expected if we assume the topography is dominantly controlled by the ringwoodite-out reaction, which has a negative Clapeyron slope (i.e. that the downwellings have a deeper associated discontinuity and the upwellings have a shallower discontinuity). The much wider spatial extent of the topography associated with downwellings on d660 compared to d410 (e.g. Western Pacific) is notable. This is explained by the greater viscosity around d660 than d410 in the geodynamic model (the viscosity in the geodynamic model starts to increase in the lower part of the mantle transition zone, so is already elevated compared to around d410 see Fig. S1).

3.2 Effect of different end-member assumptions in the local mechanical mixing calculation

One of the distinctive aspects of the method presented here compared to previous work (Papanagnou *et al.* 2023) is that we consider the effect of lateral variations of composition on discontinuity topography. We can also predict the topography by the same peak R_S method, but by assuming a fixed (mechanically mixed) composition or by assuming instead that lherzolite represents a mechanical mixture of harzburgite and basalt get a sense of the effect the local mechanical mixing and the number of end members has on the topography. The effects are small, but the discontinuities predicted using these simpler chemical assumptions have more power

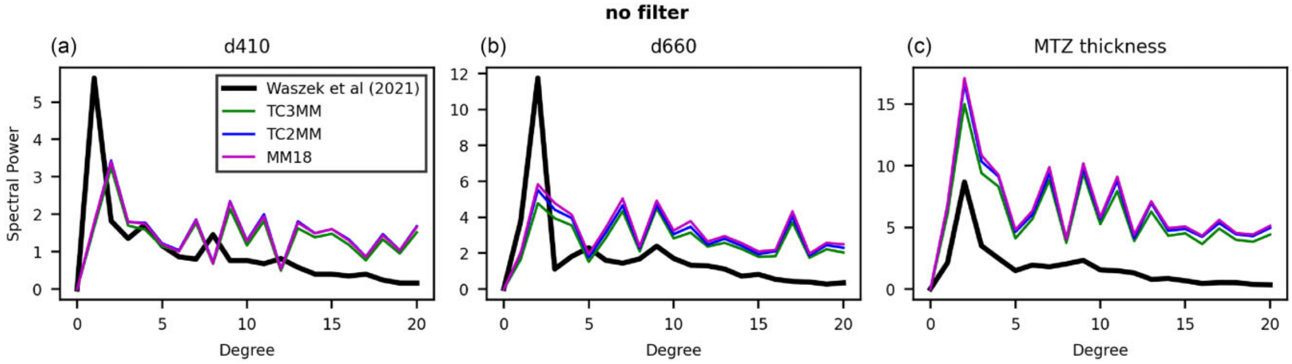

Figure 3. Power spectra of (a) 410 discontinuity topography, (b) 660 discontinuity topography, (c) MTZ thickness variations for predicted seismic structures with different mechanical mixing methods, as discussed in the text, TC3MM—local mechanical mixing with three end members, TC2MM—local mechanical mixing with two end members, MM18—global mechanical mixture. Power spectra of topography calculated by Waszek *et al.* (2021b) are included for reference.

in the spherical harmonic spectra than TC3MM at most spherical harmonic degrees (Fig. 3).

3.2.1 Reducing the number of end members to two: TC2MM

We track composition in TERRA on three end members (see above). This implicitly assumes that the entire mantle has not been completely processed since Earth's solidification, and that at the start of our model evolution (1.2 Gyr before present), a large part of it was un-processed. We can change this assumption by replacing the Lherzolite tables (representing a pyrolitic equilibrium assemblage) of seismic properties with a mechanical mixture of basalt and harzburgite, corresponding to $f_{\mathrm{bas}} = 0.2$—representing the same bulk composition but as a mixture of the two end members. We refer to this local mechanical mixing model as 'TC2MM' (since we have reduced our consideration of the thermochemical structure to a consideration of two end members). The resulting discontinuity topographies are shown in Figs 2(b), (f) and (j)—with no significant differences in the distribution of topographic anomalies. On d410, the topographic anomalies in Fig. 2(b) are generally shifted to deeper values, with a deepening of the average discontinuity depth globally. On d660 (Fig. 2f), the average discontinuity depth becomes shallower (but only by 300 m).

3.2.2 Uniform global mechanical mixture: MM18

Similarly to the section above, we can form a table representing a global mechanical mixture by mixing our end-member tables of Lhz, Hzb and Bas. A commonly assumed global mantle composition is a pyrolite model—a mechanical mixture of ∼ 20 per cent basalt and ∼ 80 per cent harzbugite—following previous work (Ritsema *et al.* 2009; Papanagnou *et al.* 2023), we use a value of $f_{\mathrm{bas}} = 0.18$ (the 'MM18' pyrolite model) for this comparison. The resulting calculated topography is shown in Figs 2(c), (g) and (k). As this global mechanical mixture has only two end-members a comparison is best made with the local mechanical mixture TC2MM. The average discontinuity depths are similar between the two models, and very few differences can be seen on d410 or d660.

3.3 Effect of bounce-point-spherical cap filter on recovered discontinuity topographies

So far, we have only calculated the geographic distribution of peak reflectivity depth and have not considered how this is observed seismically. Above (Section 2.4), we described a simple filter that captures some of the key physics, and we consider the effect of that filtering on recovered topographies here.

The topographies of d410 and d660 calculated from the MCM shown in Fig. 2 are filtered by this method and shown in Fig. 4. Note the significant reduction in the peak-to-peak amplitude of topography, and how the focused elevation of topography on the d410 beneath subduction zones in the unfiltered predicted topography is broadened to a similar width as that seen in the observed topography of d660. Fine-scale features such as the lateral offset of d410 and d660 due to steps in the surface motion patterns (e.g. beneath the Hindu-Kush) are lost. Power spectra for the filtered predicted topographies are plotted in Fig. 5. For d660 and MTZ thickness variations, filtering reduces the difference between the topographies predicted with different mixing methods (compare Figs 3 and 5), although on d410 there appears to be increased sensitivity to the filtering method. Irrespective of the mixing method, at high spherical harmonic degree the power on d410, d660 and MTZ thickness variation is significantly reduced when the 'filtering' is applied. Whilst the bounce-point-spherical-cap filtering improves the match between the predicted topographies and the topography reported by Waszek *et al.* (2021b) (compare the coloured lines to the black line in Figs 3 and 5) at high spherical harmonic degrees ($l > 7$), it does not significantly reduce the spectral power at medium spherical harmonic degree ($3 < l < 7$) or increase it at low spherical harmonic degree ($l < 3$), where there is a particularly strong mis-match between the predicted unfiltered power spectra and the seismologically observed topography structure. We might interpret this mis-match as a degree 2 structure present in the Earth but not in this MCM. For instance, we could invoke thermochemical piles swept by the history of downwellings guiding the position of upwellings or the impact of continents insulating domains of the upper mantle beneath them, but without a broader suite of MCMs it is not possible to conclude at this point. We also note that other published d410-d660 structures (e.g. Houser 2016; Guo & Zhou 2020) do not have the same dominant degree 2 structure recovered by Waszek *et al.* (2021b), so this may instead be a quirk of the averaging scheme they employ.

We illustrate the effect of varying the spherical cap radius in Fig. S7. Even with a comparatively small cap radius (250 km), the predicted topography is considerably smoothed (Figs S7a and b). With a larger cap than that which we use here in the main text (1000 km radius), topography structure is further smoothed and the peak-to-peak amplitude is slightly underpredicted and the power on high spherical harmonic degrees ($l > 7$) topography amplitude is underpredicted (Figs S7g and h).

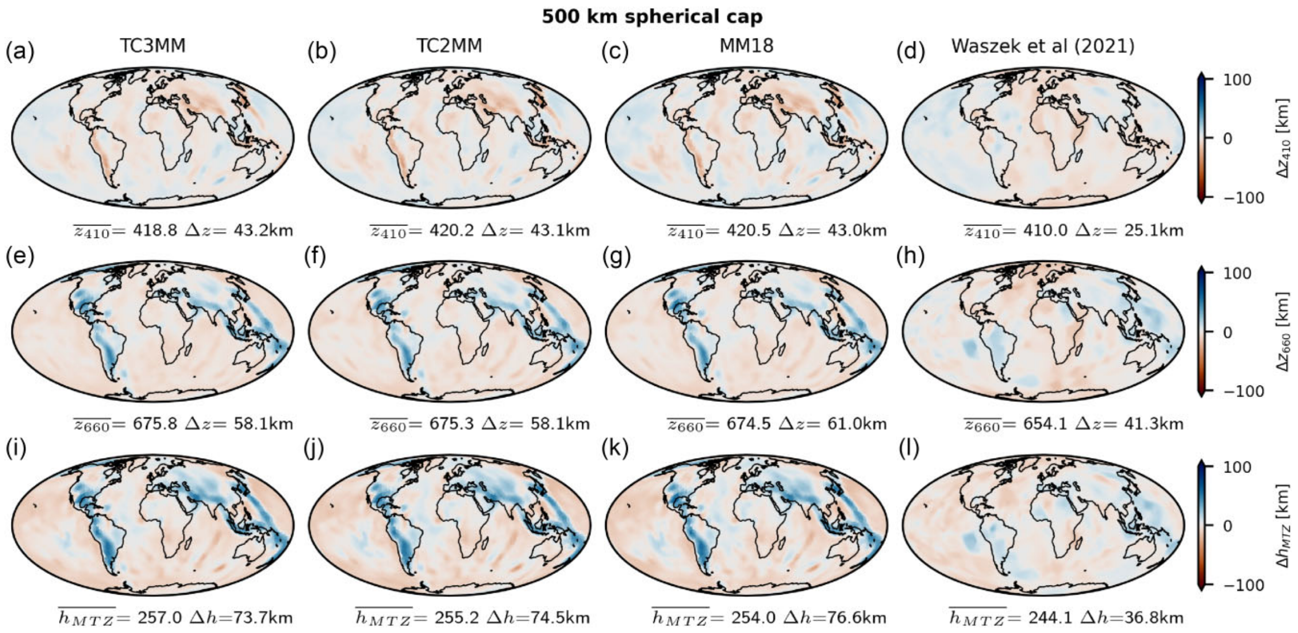

Figure 4. Topography on 410 (a–c) and 660 (e–g) discontinuities and MTZ thickness variations (i–k) calculated by the method described here, then filtered using a 500 km spherical-cap-bounce-point method, compared to the topography on 410 and 660 and MTZ thickness variations described by Waszek *et al.* (2021b) in (d), (h) and (l), respectively.

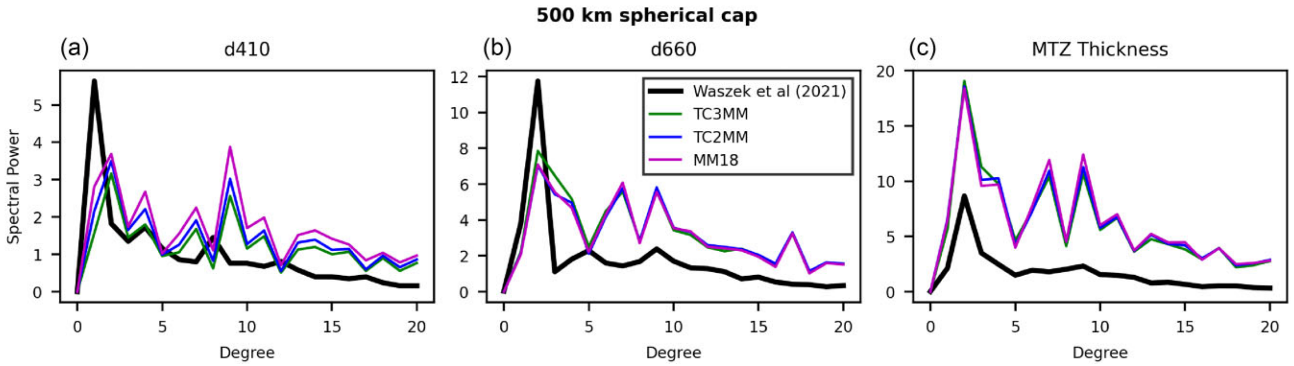

Figure 5. Power spectra of (a) 410 discontinuity topography, (b) 660 discontinuity topography (c) MTZ thickness variations for filtered predicted seismic structures with different mechanical mixing methods, as discussed in the text, TC3MM–local mechanical mixing with three end members, TC2MM–local mechanical mixing with two end members, MM18–global mechanical mixture. Power spectra of topography calculated by Waszek *et al.* (2021b) are included for reference.

Considering the variations in MTZ thickness (Fig. S7i), there is an overprediction of power at all spherical harmonic degrees for spherical caps smaller than 1000 km, and for a cap of radius 1000 km a good fit is only observed at high spherical harmonic degree ($l > 12$), where structure on d410 and d660 is completely smoothed by the cap. On d410 and d660 this largest cap predicts a spectra that matches the Waszek *et al.* (2021b) spectra from $l \sim 3$ out to $l = 20$. This suggests that the length scales of the topographies on d10 and d660 are individually reasonably correct for this large cap, but that they result in an excessively rough transition zone thickness structure—that is, that they are excessively anticorrelated for this combination of MCM and mineral physics tables.

We additionally illustrate the effect of filtering regionally in Fig. S6. Small-scale downwellings around 410 km depth, which produced narrow ridges on d410 are washed out in the filtered topography. Complex topography within the downwellings on d660 is lost, as well as the slight shallowing of the discontinuity beneath Florida and the Eastern Gulf of Mexico.

3.3.1 Predicted dip of discontinuity surfaces

Related to the short length scales of the unfiltered topography, the resulting topography has some slope everywhere but apart from in downwellings and immediately around upwellings is reasonably smooth, with slopes of less than 45°. However, the discontinuity surface is predicted to be significantly steeper (around 70° slope) around downwellings (see Fig. 6). On filtering, whilst the recovered topography is smoother, subvertical regions around upwellings and downwellings remain. The seismological significance of this will be discussed in Section 4.2.2.

3.3.2 Lateral variations in reflectivity of predicted discontinuity structures

The relative amplitude of SS precursors to the main SS arrival is also of interest since it has been used to invert for the basalt fraction in the mantle transition zone (Tauzin *et al.* 2022), and we have

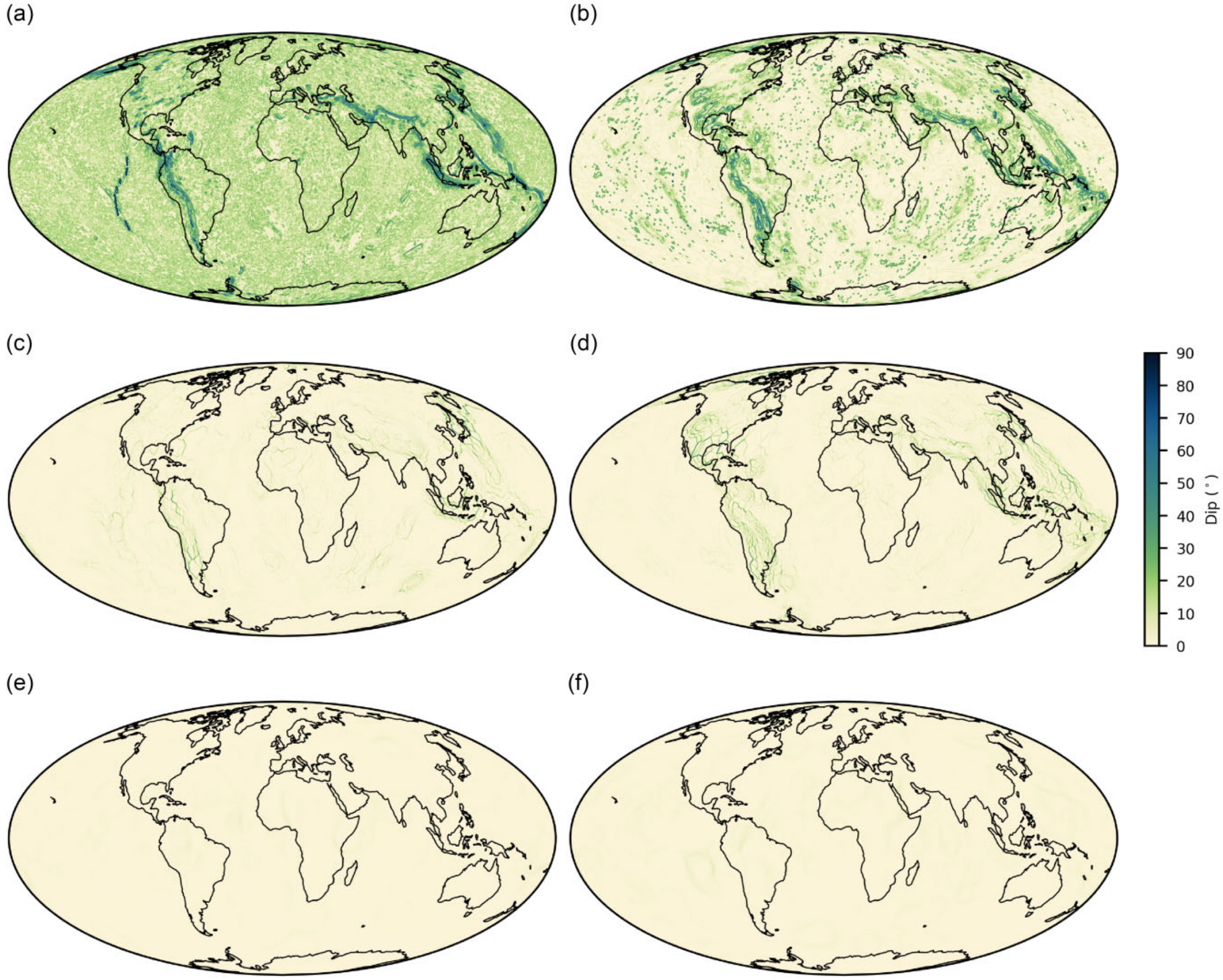

Figure 6. Dip of surface of (a, c and e) d410 and (b, d and f) d660 for unfiltered predicted topography (TC3MM) (a and b), filtered (500 km radius bounce-point spherical cap) predicted topography (c and d), Waszek *et al.* (2021b) topography model (e and f).

taken the discontinuity reflectivity as a proxy for this amplitude ratio—see discussion in Section 4.2.3. We plot the lateral distribution of peak R_S^{410} and R_S^{660} in Fig. 7. The mismatch between the geographic distribution of high R_S^d regions predicted by this simulation and areas with high SS precursor amplitudes is strong. Local mechanical mixing is more important in local variations in R_S^d structure than for the discontinuity topography, with the 'bright' spots around upwellings less intense, and more short-wavelength structure notable (Fig. S8) than in the reflectivity structure predicted from a global mechanical mixture. The variations we find here in d660 reflectivity due to variations in the thermal structure of the MCM are of a similar magnitude to those interpreted to be due to chemical variations within the mantle, but have a different geometry—being aligned along downwelling and upwelling centres, unlike in the Waszek *et al.* (2021b) data set where high amplitude regions are not obviously associated with the location of slabs or large plumes in the Earth. The variations in the reflectivity of d410 are smaller than on d660, but again are closely associated with the distribution of downwellings and upwellings in the MCM. We expand on the significance of the reflectivity variations in Section 4.2.3

4 DISCUSSION

4.1 Comparison to previous work predicting d410 and d660 from MCMs

Papanagnou *et al.* (2023) also predicted d410 and d660 topography from a MCM, in their case a model published by Nerlich *et al.* (2016), which has a higher resolution than the MCM used here, allowing Nerlich *et al.* to use an upper mantle viscosity of 1×10^{21} Pa s, a quarter of that we use here, in line with the Haskell constraint and likely resulting in thermal anomalies that are narrower and smaller in amplitude than in the simulation we have used from Davies *et al.* (2025). Their CMB temperature is also significantly higher (4200 K versus 4007 K here), which may explain why the depression of d660 they predict in upwelling centres due to the garnet-out control of the d660 is not present in our predicted topographies. Since Papanagnou *et al.* (2023) did not consider the resolution of the SS-precursor or lateral chemical heterogeneity, a comparison is made with the unfiltered topographies with the global mechanical mixture 'MM18' in Figs 2(c), (g) and (k). If the filtering scheme used here were to be applied to the topographies predicted

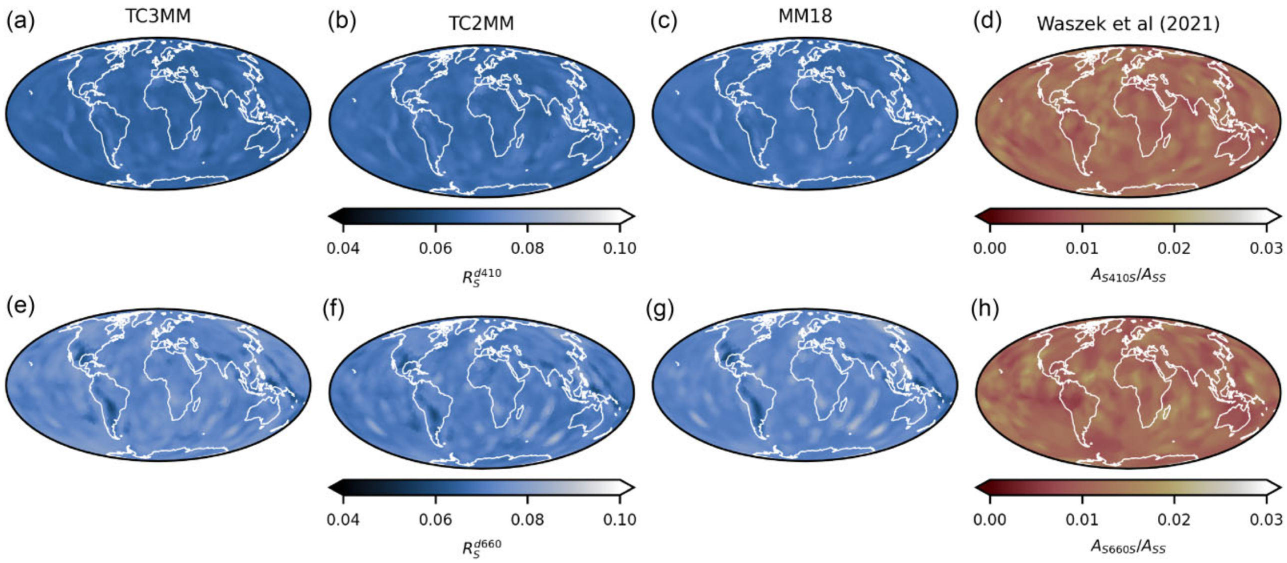

Figure 7. R_S (Shear wave reflectivity) on d410 (a–c) and d660 (e–g) for each of the mechanical mixing methods considered in this paper TC3MM (a and e), TC2MM (b and f) and MM18 (c and g) are compared qualitatively to the amplitude of the SS precursor (d and h), filtered using the bounce-point spherical cap of radius 500 km (and 'thickness' of 30 km. Note the poor fit in geographic distribution between the geodynamic predictions and the data of Waszek *et al.* (2021b). The average reflectivities of d410 and d660 are more different (e.g. for TC3MM 0.066 and 0.073 respectively) than the average normalized amplitude of the precursors in the Waszek *et al.* data set (0.038 and 0.037 respectively).

by Papanagnou *et al.* (2023), we would expect the extremely localized deflections of the discontinuities to be spread out, and in particular the shallowing of the d660 in the upwelling cores are unlikely to be recovered by this filter. Spectrally, we would not expect the topographies predicted by Papanagnou *et al.* (2023) to provide a markedly improved fit to the Waszek *et al.* data set due to the comparatively low power at degree two on both discontinuities for the comparable mantle composition of MM18 (their Fig. S11).

The depth anomaly ranges quoted in the figure are from the 0.1-st percentile to the 99.9-th percentile, and with reference to Fig. S19 of Papanagnou *et al.* (2023), we predict slightly broader ranges of discontinuity depths than they do, which is not surprising considering the higher viscosity used in the MCM of this study. Plotting a histogram of the topography on d410 and d660 for the unfiltered MM18 model in Fig. S13 we can make a more detailed comparison to the topographies predicted by Papanagnou *et al.* (2023). The range and distribution of predicted depths of d410 predicted by us from the geodynamic model 'm_cc_066_u' (Davies *et al.* 2024) (Fig. S13) is very similar to that predicted by Papanagnou *et al.* (2023) (their Fig. S19) for a less viscous mantle for a similar mantle composition. Histograms of d660 depths are more different than for d410 with our topography distribution extending to greater depths than that which Papanagnou *et al.* (2023) predict for the same composition and their mantle circulation model. This likely is due to the detail of the viscosity structures used in the geodynamic simulations; whilst usually described as a 'jump at 660 km depth', due to the finite resolution in mantle convection or circulation models it is always necessary for this jump to be spread over several radial grid nodes. Davies *et al.* (2025) chose to implement this so that the jump to the lower mantle viscosity is completed at 660 km depth (i.e. the viscosity at d660 is $\sim 1.2 \times 10^{23}$ Pa s), whereas Nerlich *et al.* (2016) chose to implement the jump so that it is centred on 660 km depth (i.e. the viscosity at d660 is only $\sim 6 \times 10^{21}$ Pa s, and so the convective temperature anomalies will be smaller and more localized than around d660 in m_cc_066_u, which is reflected in the tighter range of depths predicted by Papanagnou *et al.* (2023) for d660). This choice in radial viscosity structure, rather than the factor of four difference in reference viscosity, has a larger effect on the predicted discontinuity topographies and in particular in explaining the difference in predicted d660 depth-frequency distribution and range between this work and that of Papanagnou *et al.* (2023).

4.2 Comparison to SdS-derived topography

For global geodynamic simulations, the natural point of comparison are global SS-precursor topographies (e.g. Houser 2016; Guo & Zhou 2020; Waszek *et al.* 2021b). As an example we here make a comparison to the topography model of Waszek *et al.* (2021b), derived from SS precursors in seismograms filtered for a period of $15 - 50$ s. A naive comparison between our calculated topographies in the geographic (Fig. 2) and spectral domains (Fig. 3) is not encouraging—our peak-to-peak topography is much larger ($\sim$ 100 km on d410 and d660) than that found by Waszek *et al.* (2021b) ($\sim$ 28 km and $\sim$ 45 km respectively), and our structure is focused on short-wavelengths (high spherical harmonic degree) particularly around downwellings.

4.2.1 Influence of bounce point spherical cap filter on d410 and d660 structure

The topography that we naively predicted from a mantle circulation with a lateral temperature range of $\sim$ 2000 K in the MTZ that drives vigorous convection compared poorly to the topography recovered from SS-precursors ($\sim$ 100 km on each of d410 and d660, 150 km on the transition zone thickness variations compared to $\sim$ 40 km observed on all three in recent studies (e.g. Houser 2016; Guo & Zhou 2020; Waszek *et al.* 2021b). However, when a seismologically motivated cap of radius 500 km is applied, the topographies become of similar amplitude to those inverted by Waszek *et al.* (2021b) and Tauzin *et al.* (2022) to a much smaller temperature range of 400 K. Of course, this is dependent on the cap size, and many models in principle could be oversmoothed until they are compatible with observations, but given the contribution to total sensitivity away from the first Fresnel zone is small with increasing radius (e.g. Guo & Zhou 2020, fig. 4) doing this would not be seismologically motivated. We note that the range of depths for d410 and d660 when filtered with the largest cap in Fig. S7 are within a couple of kilometres of the ranges for d410 and d660 reported by Waszek *et al.* (2021b).

4.2.2 Predicted discontinuity topography extremely steep around downwellings

We highlighted the steep dips on the d410 and d660 predicted topography surfaces (see Section 3.3.1). Here we sketch some seismologic implications. Such a steep discontinuity topography structure could significantly complicate the physics of reflection, potentially changing the location of bounce-points away from the mid-point of the source–receiver great circle (e.g. Rochira & Thomas 2023) and significantly changing the reflectivity-offset curve. Whilst the global topographies inverted in SS-precursor studies, such as the Waszek *et al.* (2021b) model we compare to here, are smooth and rolling (dips not exceeding 15°) there is some evidence that the discontinuity surface in the Earth could be considerably rougher, at least in places. Rochira & Thomas (2023) showed that some SS and PP precursors that could be interpreted as reflectors in the deeper mid-mantle (e.g. Waszek *et al.* 2018) were, when the backazimuth was taken into account in the bounce-point location, more accurately located around d410 and d660. Whilst these out-of-plane reflections could be due to compositional or thermal structure associated with the downwelling in the study region, SdS reflected out of the great-circle plane is also a possibility (Rochira & Thomas 2023). Neele *et al.* (1997) and Neele & Regt (1999) considered the topography of a discontinuity around slabs with a similar magnitude to that presented here, showing the smearing of the intense deflection away from the slab regions they were imposed within, also creating effects far from the downwelling slab. However, the deflections in unfiltered discontinuity topography we predict are much steeper than the sinusoidal topographies used by Neele *et al.*, and we expect significant deflections both due to slabs and upwellings. To properly assess the validity of the simple spherical cap filter, we would need to propagate seismic waves through regions of our predicted mantle transition zone reflectivity structures to see what structures are recovered, compared to the ‘filtered’ topographies presented here.

4.2.3 Significance of lateral reflectivity variations in the Earth and predicted discontinuity structures

Tauzin *et al.* (2022) use the observed variations of MTZ thickness and the amplitude of SS precursors to invert for the thermochemical structure—principally using MTZ thickness variations to recover temperature and the amplitude of the SS-precursor for basalt fraction. However, we find significant variations in discontinuity reflectivity due to thermal variations (see Fig. 7 and Fig. S8).

The relative amplitude of the SS precursor phase should be mainly controlled by the reflectivity of the discontinuity, that we used for the prediction of the depth of the discontinuities, but is also controlled by any attenuation along the ray-path, which is not trivial to assess. For now, we accept R_s^d as a proxy for A_{SdS}/A_{SS}, but note these potential sources of error. Another major component is the variation of angle of incidence of the SS-precursor with the discontinuity surface, either due to variation in the source–receiver separation (which Waszek *et al.* correct for in their reported SS-precursor amplitude model), or the variation in the dip of the discontinuity (which we do not consider in this analysis, since where this is important more complex wavefront-healing physics may also be in play). Interrogating our tables we produce a similar relationship between MTZ thickness and R_S for varying f_{bas} and T as found by Tauzin *et al.* (2022) (Fig. S10)—which suggests that using R_S^{410} or R_S^{660} as an initial proxy for SS precursor amplitudes is not unreasonable.

The average reflection amplitude of S410S and S660S is similar in the Waszek *et al.* (2021b) data set (d410 is 2.5 per cent brighter than d660), but in the discontinuity structure predicted from this simulation, d660 is significantly (10 per cent) brighter than d410, using the three-end-member mechanical mixing (TC3MM, Fig. 7). Varying the fraction of basalt in a global mechanical mixture (Fig. S8) allows $R_S^{660} \sim R_S^{410}$ where $f_{\mathrm{bas}}^{660} > f_{\mathrm{bas}}^{410}$. This geodynamic model does not have an accumulation of enriched material in the mantle transition zone around d660, but this suggests that a better fit to the Earth may be observed for a geodynamic simulation with basalt enrichment in the basalt density filter (e.g. Davies 2008; Yan *et al.* 2020).

Plotting histograms of SdS amplitude from the Waszek *et al.* (2021b) model and values of R_S^d predicted for this geodynamic model (Fig. S11), we highlight how the reflectivity is much less variable for the predicted discontinuities than the observed precursor amplitudes. This could suggest that this geodynamic simulation underestimates the compositional variability in the mantle transition zone, particularly given the range of reflectivity predicted for the various global mechanical mixtures (see Fig. S12). Further, given our overprediction of the relative reflectivity of d660, it appears very likely that there are regions with additional basaltic material in the Earth’s mantle transition zone, as has been found from previous seismological work (Cammarano *et al.* 2009; Khan *et al.* 2009; Munch *et al.* 2020; Bissig *et al.* 2022; Tauzin *et al.* 2022). Other factors, such as the roughness of the discontinuity surface may also play an important role (see above).

4.3 Relative importance of thermal and compositional heterogeneity for discontinuity topography

When considering the predicted topographies by this method (Fig. 2) for a MCM with moderate compositional variations we find that the local mechanical mixing has essentially no effect, particularly once filtered for what is seismically visible (Fig. 4). We do show some subtle differences in the reflectivity structure for discontinuities picked from different mixing assumptions (Fig. 7), but in the model we have shown here there is not a drastic difference for the different assumptions about composition mixing.

If we vary the composition of the whole mantle according to different proportions of basalt and ‘pyrolite’ in a global mechanical mixture in the range of $0.1 < f_{\mathrm{bas}} < 0.5$ we see no significant change in predicted filtered topographies (see Fig. S9), highlighting that for moderate changes in mantle composition, any changes are limited to changes in lateral reflectivity structure.

This highlights that for reasonable mantle transition zone compositions, d410 and d660 topographies predicted from a mantle circulation model are explained principally by the decomposition of olivine and ringwoodite (not precluding a role for other reactions at extremes of temperature), and that the reflectivity is affected by the relative abundance of enriched basaltic material which controls the relative importance of the garnet-out reaction compared to the ringwoodite-out reaction.

4.4 Is MTZ discontinuity structure a useful constraint on MCMs?

4.4.1 Topography of d410 and d660

Fitting the observed topographies of d410 and d660 in the Earth from a MCM is a complex combination of thermochemical structure, the correct application of mineral physics tables and any seismological filtering. We have shown that a very simple seismology-motivated smoothing filter obscures a lot of the fine detail of topography structure expected from a geodynamical simulation, and have discussed the dominance of thermal structure as a control on d410 and d660 structure rather than composition for moderate variations in basalt content.

The thermal structure of the mid-mantle is dominated by downgoing slabs and upwelling plumes, and is also expected to control the transition zone discontinuity structure. The location and morphology of the downgoing slabs are largely a function of the surface motion history, which in MCMs is imposed at the surface. However, the remainder of the thermal structure is a function of the reaction of the convecting mantle to the imposed downwellings and does vary between geodynamic models with different dynamic structures, particularly variations in rheology and mineral physics. The geodynamic significance of interpretations of the topographies of individual discontinuities is disputed, due to the potential dominance of uncorrected upper mantle velocity structure in the differential traveltimes of the SS and SdS phases (e.g. Tauzin *et al.* 2022). This makes it challenging to interpret poorly fitting (geographically or spectrally) predicted individual topographies in terms of geodynamics.

4.4.2 Variations in MTZ thickness

As the transition zone thickness is determined by the differential traveltimes of S660S and S410S, without reference to the SS phase, it should not be sensitive to upper mantle velocity structure variations (e.g. Tauzin *et al.* 2022). Sadly this approach limits the ability to consider separately the thermal structure at 410 and 660 km depth, although generally the offset in convective thermal structures between 410 and 660 km depth is generally expected to be small compared to the 1000 km width of the SS precursors' first Fresnel zone. This potentially suggests that variations of transition zone thickness can give a sense of the fit between the simulated and true Earth's lateral thermal structure at the scale lengths SS precursors are sensitive to. However S410S-S660S differential traveltime may not be a simple proxy for MTZ thickness as Koroni *et al.* (2017) showed S410S has significant sensitivity to discontinuity structure at 670 km depth, although this was at longer periods than those used by SS-precursor studies. We do not consider this further here, but note that it is still worth considering d410 and particularly d660 individually in addition to the transition zone thickness.

4.4.3 Reflection amplitude structure

Fit to reflection amplitude structure is more complex—as reflection amplitude structure has a strong compositional component, it is sensitive to the long-term evolution and residence of melt-derived heterogeneity in the lower mantle transition zone (Tauzin *et al.* 2022). The amount and distribution of basaltic material at the base of the MTZ should be a function of the history of melt-production, history of convection, the relative behaviours of enriched and depleted material in the MTZ, other heterogeneities in the mantle, as well as the uncertainties in mineral physics and seismological filtering of the mantle transition zone. However, even in a well mixed mantle such as that produced by this MCM, lateral variations in R_S^d exist, largely driven by thermal structure instead of compositional variations. Therefore, lateral variations in reflectivity may be a more discriminating metric than the discontinuity depth variations, and so a well fitting MCM may not emerge until our knowledge of mid-mantle dynamics, mineral physics and seismology is much improved.

4.4.4 Characteristics of an Earth-like MCM

If an Earth-like MCM were found, the resulting discontinuity structure when filtered for the sensitivity of SS precursors should match the predicted depths of d410 and d660, as well as the amplitude of the discontinuity topographies and transition zone thickness. The spherical harmonic spectra of the predicted discontinuities should peak on degree 1 or 2 and then decay approximately monotonically with increasing spherical harmonic degree. These reflect the correct thermal structure globally (average discontinuity depths) and the correct lateral variations of temperature (discontinuity topographies). From the predicted reflectivity structure the global distribution of 'bright' and 'dark' spots should match the reported amplitude structure, indicating a reasonable thermochemical structure. However, we anticipate this as a challenging metric to match since the amplitude of reflected waves is a function of the thermal and chemical structures (the latter of which is sensitive to the history of the delivery of compositional heterogeneity to the mantle transition zone), and is possibly more sensitive to the correct 'seismological treatment' than the discontinuity topographies.

4.4.5 Limitations of the candidate model

Whilst we do predict the mean depths of d410 and d660 well, we overpredict the topography on both discontinuities (by a factor of about 1.7 for d410 and 1.5 for d660). The thickness of the MTZ is slightly overpredicted, as are the range of MTZ thickness variations. Spherical harmonic power is overpredicted at high degree for d410 and d660, and underpredicted at low degree, but the power of MTZ thickness variation spectra is overpredicted at all degrees. We suggest this reflects an excessive anticorrelation of d410 and d660 predicted by this method from this MCM compared to those recovered form the Earth using SS precursors. This suggests a poor match between the thermal structures of our MCM and Earth's. However, there are many regions where the distribution of thick and thin regions of the MTZ is encouraging (see Fig. 4).

The comparison between the predicted reflectivity structure and the amplitude structure is less straight-forward. We do not consider the reflectivity of the Earth's surface underside. Similar to the effect of shallow structure on traveltimes, the reflectivity of the Earth's surface could be highly dependent on regions of partial melt, the thickness of lithosphere or crust, the presence of oceans and icecaps and the roughness of surface topography. However, we do not correctly predict the relationship between the mean reflectivity values of d410 and d660, which the Waszek *et al.* data suggest are similar, but with d410 slightly brighter than d660. We predict d660 as slightly brighter than d410, which might reflect the underprediction of basalt fraction around 660 km depth in this simulation.

Whilst this assessment has shown that m_cc_066_u is not an ideal geodynamic model, it highlights the utility of considering the discontinuity topography as we have here, as it has allowed us to take a mantle circulation model that is fairly reasonable (Davies *et al.* 2025) and critically assess its mantle transition zone structure and potentially informs the parameter space where we might seek a better-fitting model.

5 CONCLUSION

We predict the topography of d410 and d660 for a thermochemical MCM. The Fresnel Zone of SS precursors has a significant impact on the recovered topography, and when we apply a simple filter to our predicted topographies we can compare the predicted topographies of d410 and d660 to those inverted from SS precursors meaningfully. Lateral chemical variations seem to have a limited role in controlling the topography predicted from a well-mixed thermochemical MCM, although appear important in explaining the discontinuity reflectivity structure.

We assessed a candidate mantle circulation model using its discontinuity topography and reflectivity structure, finding the range of discontinuity depths were too large on both d410 and d660 and that reflectivity structure predicted from this model does not match global observations well. This is interpreted as suggesting a smaller range of temperatures and more recycled heterogeneity in the MTZ than in our geodynamic model considered here. This allowed us to critically assess the discontinuity structure predicted from a MCM, suggesting that either the thermochemical structure is not Earth-like or that the simple treatment of the SS-precursor interaction with the discontinuities we used here is not sufficient. We also note that the discontinuities predicted from this geodynamic simulation are much rougher than the sub-horizontal discontinuities recovered by SS-precursor studies from the Earth and expect this could have some impact on the observation of the discontinuities.

ACKNOWLEDGMENTS

We thank Christine Houser and an anonymous reviewer, whose feedback improved this paper. This work used the ARCHER2 UK National Supercomputing Service (https://www.archer2.ac.uk) for all geodynamic simulations. All maps have been produced using Cartopy (Met Office 2010-2025). All colourmaps are taken or adapted from Crameri *et al.* (2020). All spherical harmonic routines accomplished using pyshtools (Wieczorek & Meschede 2018). GTM is funded by the College of Physical Sciences and Engineering, Cardiff University. JHD, RM, JW and JP are funded by the NERC large grant 'MC^2—Mantle Circulation Constrained' (grant codes NE/T012633/1 and NE/T012595/1). This is Cardiff EARTH CRediT contribution 51.

SUPPORTING INFORMATION

Supplementary data are available at *GJIRAS* online.

suppl_data

DATA AVAILABILITY

The thermochemical field of the mantle circulation model m_cc_066_u is available for download via Zenodo (Davies *et al.* 2024,available at https://doi.org/10.5281/zenodo.13960492), and similar mineral-physics tables are released there. The topographies were calculated using Python3 codes 'TERRA-tumulus' released publicly here: https://doi.org/10.5281/zenodo.15630096. We compared our topographies to the model released by Waszek *et al.* (2021b) available via the ISC's Seismological Data set Repository [Waszek *et al.* 2021a, available at https://doi.org/10.31905/7M3LMG8X)].

REFERENCES

Agius, M.R., Rychert, C.A., Harmon, N., Tharimena, S. & Kendall, J.M., 2021. A thin mantle transition zone beneath the equatorial Mid-Atlantic Ridge, *Nature,* **589**(7843), 562–566.

Baker, M.B. & Beckett, J.R., 1999. The origin of abyssal peridotites: a reinterpretation of constraints based on primary bulk compositions, *Earth planet. Sci. Lett.,* **171**(1), 49–61.

Baumgardner, J.R., 1983. *A Three-Dimensional Finite Element Model for Mantle Convection,* University of California, Los Angeles.

Birch, F., 1952. Elasticity and constitution of the Earth's interior, *J. geophys. Res. (1896-1977),* **57**(2), 227–286.

Bissig, F., Khan, A. & Giardini, D., 2022. Evidence for basalt enrichment in the mantle transition zone from inversion of triplicated *P*- and *S*-waveforms, *Earth planet. Sci. Lett.,* **580,** 117387.

Bonatto, L., Schlaphorst, D., Silveira, G., Mata, J., Civiero, C., Piromallo, C. & Schimmel, M., 2024. Unveiling the distinct structure of the upper mantle beneath the Canary and Madeira Hotspots, as depicted by the 660, 410, and X discontinuities, *J. geophys. Res.: Solid Earth,* **129**(5), e2023JB028195.

Bunge, H.-P. & Baumgardner, J.R., 1995. Mantle convection modeling on parallel virtual machines, *Comput. Phys.,* **9**(2), 207.

Bunge, H.P., Richards, M.A. & Baumgardner, J.R., 1997. A sensitivity study of three-dimensional spherical mantle convection at 108 Rayleigh number: effects of depth-dependent viscosity, heating mode, and an endothermic phase change, *J. geophys. Res.: Solid Earth,* **102**(6), 11 991–12 007.

Burky, A.L., Irving, J.C. & Simons, F.J., 2023. The mantle transition zone beneath eastern North America: Receiver functions and tomographic velocity models, *Phys. Earth planet. Inter.,* **340,** 107035.

Cammarano, F., Romanowicz, B., Stixrude, L., Lithgow-Bertelloni, C. & Xu, W., 2009. Inferring the thermochemical structure of the upper mantle from seismic data, *Geophys. J. Int.,* **179**(2), 1169–1185.

Chambers, K., Deuss, A. & Woodhouse, J.H., 2005. Reflectivity of the 410-km discontinuity from PP and SS precursors, *J. geophys. Res.: Solid Earth,* **110**(B2).

Chevrot, S., Vinnik, L. & Montagner, J.-P., 1999. Global-scale analysis of the mantle Pds phases, *J. geophys. Res.: Solid Earth,* **104**(B9), 20203–20219.

Christensen, U.R. & Yuen, D.A., 1985. Layered convection induced by phase transitions., *J. geophys. Res.,* **90**(B12).

Clauser, C. & Huenges, E., 1995. Thermal Conductivity of Rocks and Minerals, in *A Handbook of Physical Constants: Rock Physics and Phase Relations,* Vol. **3,** pp.105–126, ed. Ahrens, T.J., AGU Reference Shelf Series.

Collier, J.D. & Helffrich, G.R., 2001. The thermal influence of the subducting slab beneath South America from 410 and 660 km discontinuity observations, *Geophys. J. Int.,* **147**(2), 319–329.

Connolly, J.A.D., 2009. The geodynamic equation of state: What and how, *Geochem. Geophys. Geosyst.,* **10**(10).

Cottaar, S. & Deuss, A., 2016. Large-scale mantle discontinuity topography beneath Europe: signature of akimotoite in subducting slabs, *J. geophys. Res.: Solid Earth,* **121**(1), 279–292.

Crameri, F., Shephard, G.E. & Heron, P.J., 2020. The misuse of colour in science communication, *Nat. Commun.,* **11**(1), 5444.

Dahlen, F.A., 2005. Finite-frequency sensitivity kernels for boundary topography perturbations, *Geophys. J. Int.,* **162**(2), 525–540.

Davies, C.J., 2015. Cooling history of Earth’s core with high thermal conductivity, *Phys. Earth planet. Inter.,* **247,** 65–79.

Davies, G.F., 2008. Episodic layering of the early mantle by the ‘basalt barrier’ mechanism, *Earth planet. Sci. Lett.,* **275**(3–4), 382–392.

Davies, J.H.& *et al.*., 2024. *How to assess similarities and differences between mantle circulation models and earth using disparate independent observations: Data and analysis,* Zenodo.

Davies, J.H. *et al.*, 2025. How to assess similarities and differences between mantle circulation models and Earth using disparate independent observations, *Proc. R. Society A: Mathematical, Physical and Engineering Sciences,* **481**(2315), 20240827.

Deuss, A., Redfern, S. A.T., Chambers, K. & Woodhouse, J.H., 2006. The nature of the 660-kilometer discontinuity in Earth’s Mantle from global seismic observations of *PP* precursors, *Science,* **311**(5758), 198–201.

Flanagan, M.P. & Shearer, P.M., 1998. Global mapping of topography on transition zone velocity discontinuities by stacking SS precursors, *J. geophys. Res.: Solid Earth,* **103**(B2), 2673–2692.

Glasgow, M.E., Zhang, H., Schmandt, B., Zhou, W.-Y. & Zhang, J., 2024. Global variability of the composition and temperature at the 410-km discontinuity from receiver function analysis of dense arrays, *Earth planet. Sci. Lett.,* **643,** 118889.

Goes, S., Cammarano, F. & Hansen, U., 2004. Synthetic seismic signature of thermal mantle plumes, *Earth planet. Sci. Lett.,* **218**(3–4), 403–419.

Goes, S., Yu, C., Ballmer, M.D., Yan, J. & van der Hilst, R.D., 2022. Compositional heterogeneity in the mantle transition zone, *Nat. Rev. Earth Environ.,* **3**(8), 533–550.

Gu, Y., Dziewonski, A.M. & Agee, C.B., 1998. Global de-correlation of the topography of transition zone discontinuities, *Earth planet. Sci. Lett.,* **157,** 57–67.

Gu, Y.J., Dziewoński, A.M. & Ekström, G., 2003. Simultaneous inversion for mantle shear velocity and topography of transition zone discontinuities, *Geophys. J. Int.,* **154**(2), 559–583.

Guo, Z. & Zhou, Y., 2020. Finite-frequency imaging of the global 410- and 660-km discontinuities using SS precursors, *Geophys. J. Int.,* **220**(3), 1978–1994.

Heister, T., Dannberg, J., Gassmöller, R. & Bangerth, W., 2017. High accuracy mantle convection simulation through modern numerical methods - II: Realistic models and problems, *Geophys. J. Int.,* **210**(2), 833–851.

Houser, C., 2016. Global seismic data reveal little water in the mantle transition zone mantle phase transitions, *Earth planet. Sci. Lett.,* **448,** 94–101.

Houser, C. & Williams, Q., 2010. Reconciling Pacific 410 and 660km discontinuity topography, transition zone shear velocity patterns, and mantle phase transitions, *Earth planet. Sci. Lett.,* **296**(3–4), 255–266.

Houser, C., Masters, G., Flanagan, M. & Shearer, P., 2008. Determination and analysis of long-wavelength transition zone structure using SS precursors, *Geophys. J. Int.,* **174**(1), 178–194.

Huang, Q., Schmerr, N., Waszek, L. & Beghein, C., 2019. Constraints on Seismic Anisotropy in the Mantle Transition Zone From Long-Period SS Precursors, *J. geophys. Res.: Solid Earth,* **124**(7), 6779–6800.

Ito, E., Takahashi, E. & Matsui, Y., 1984. The mineralogy and chemistry of the lower mantle” an implication of the ultrahigh-pressure phase relations in the system MgO-FeO-SiO 2, *Earth planet. Sci. Lett.,* **67,** 238–248.

Jeffreys, H. & Bullen, K.E., 1940. *Seismological Tables,* Tech. rep., British Association Seismological Committee, London.

Jenkins, J., Cottaar, S., White, R.S. & Deuss, A., 2016. Depressed mantle discontinuities beneath Iceland: Evidence of a garnet controlled 660 km discontinuity?, *Earth planet. Sci. Lett.,* **433,** 159–168.

Keifer, I. & Dueker, K., 2019. Testing the hypothesis that temperature modulates 410 and 660 discontinuity topography beneath the eastern United States, *Earth planet. Sci. Lett.,* **524**.

Khan, A., Boschi, L., &, 2009. On mantle chemical and thermal heterogeneities and anisotropy as mapped by inversion of global surface wave data, *J. geophys. Res.: Solid Earth,* **114**(B9).

Koroni, M., Bozdağ, E., Paulssen, H. & Trampert, J., 2017. Sensitivity analysis of seismic waveforms to upper-mantle discontinuities using the adjoint method, *Geophys. J. Int.,* **210**(3), 1965–1980.

Kronbichler, M., Heister, T. & Bangerth, W., 2012. High accuracy mantle convection simulation through modern numerical methods: high accuracy mantle convection simulation, *Geophys. J. Int.,* **191**(1), 12–29.

Laske, G., Masters, G., Ma, Z. & Pasyanos, M., 2012. CRUST1.0: An Updated Global Model of Earth’s Crust, in *Geophysical Research Abstracts,* Vol. **14,** pp. EGU2012–3743-1, EGU, Vienna, Austria.

Lawrence, J.F. & Shearer, P.M., 2008. Imaging mantle transition zone thickness with *SdS* - *SS* finite-frequency sensitivity kernels, *Geophys. J. Int.,* **174**(1), 143–158.

Lee, S.-H., Rhie, J., Park, Y. & Kim, K.-H., 2014. Topography of the 410 and 660 km discontinuities beneath the Korean Peninsula and southwestern Japan using teleseismic receiver functions, *J. geophys. Res.: Solid Earth,* **119**(9), 7245–7257.

Liu, Z., Li, J. & Kong, F., 2023. Topographic variations of mantle transition zone discontinuities in the Java subduction zone and adjacent regions from receiver function analyses, *Tectonophysics,* **849,** 229723.

Maguire, R., Ritsema, J., Van Keken, P.E., Fichtner, A. & Goes, S., 2016. *P* - and *S* -wave delays caused by thermal plumes, *Geophys. J. Int.,* **206**(2), 1169–1178.

Maguire, R., Ritsema, J. & Goes, S., 2018. Evidence of subduction-related thermal and compositional heterogeneity below the United States from transition zone receiver functions, *Geophys. Res. Lett.,* **45**(17), 8913–8922.

Met Office, 2010-2025. *Cartopy: a cartographic Python library with a Matplotlib interface*. Available at: https://cartopy.readthedocs.io/stable/citation.html

Muir, J. M.R., Zhang, F. & Brodholt, J.P., 2021. The effect of water on the post-spinel transition and evidence for extreme water contents at the bottom of the transition zone, *Earth planet. Sci. Lett.,* **565,** 116909.

Munch, F.D., Khan, A., Tauzin, B., Van Driel, M. & Giardini, D., 2020. Seismological evidence for thermo-chemical heterogeneity in Earth’s continental mantle, *Earth planet. Sci. Lett.,* **539,** 116240.

Müller, R.D. *et al.*, 2022. A tectonic-rules-based mantle reference frame since 1 billion years ago - implications for supercontinent cycles and plate–mantle system evolution, *Solid Earth,* **13**(7), 1127–1159.

Neele, F. & Regt, H.D., 1999. Imaging upper-mantle discontinuity topography using underside-reflection data, *Geophys. J. Int.,* **137**(1), 91–106.

Neele, F., Regt, H. & Decar, J., 1997. Gross errors in upper-mantle discontinuity topography from underside reflection data, *Geophys. J. Int.,* **129**(1), 194–204.

Nerlich, R., Colli, L., Ghelichkhan, S., Schuberth, B. & Bunge, H.-P., 2016. Constraining central Neo-Tethys Ocean reconstructions with mantle convection models, *Geophys. Res. Lett.,* **43**(18), 9595–9603.

Ohtani, E., 2021. Hydration and dehydration in Earth’s interior, *Annu. Rev. Earth planet. Sci.,* **49**(1), 253–78.

Panton, J., 2020. *Advances in using Three-Dimensional Mantle Convection Models to Address Global Geochemical Cycles,* Ph.D. thesis, Prifysgol Caerdydd Cardiff University.

Panton, J., Davies, J.H., Elliott, T., Andersen, M., Porcelli, D. & Price, M.G., 2022. Investigating Influences on the Pb Pseudo-Isochron Using Three-Dimensional Mantle Convection Models With a Continental Reservoir, *Geochem. Geophys. Geosyst.,* **23**(8), e2021GC010309.

Papanagnou, I., Schuberth, B. S.A. & Thomas, C., 2023. Geodynamic predictions of seismic structure and discontinuity topography of the mantle transition zone, *Geophys. J. Int.,* **234**(1), 355–378.

Pasyanos, M.E., Masters, T.G., Laske, G. & Ma, Z., 2014. LITHO1.0: An updated crust and lithospheric model of the Earth, *J. geophys. Res.: Solid Earth,* **119**(3), 2153–2173.

Rao, B.P., Kumar, M.R. & Saikia, D., 2020. Seismic Evidence for a Hot Mantle Transition Zone Beneath the Indian Ocean Geoid Low, *Geochem. Geophys. Geosyst.,* **21**(7), e2020GC009079.

Revenaugh, J. & Jordan, T.H., 1991. Mantle layering from ScS reverberations: 2. The transition zone, *J. geophys. Res.: Solid Earth,* **96**(B12), 19 763–19 780.

Ringwood, A. & Major, A., 1970. The system Mg2SiO4-Fe2SiO4 at high pressures and temperatures, *Phys. Earth planet. Inter.,* **3,** 89–108.

Ritsema, J., Xu, W., Stixrude, L. & Lithgow-Bertelloni, C., 2009. Estimates of the transition zone temperature in a mechanically mixed upper mantle, *Earth planet. Sci. Lett.,* **277**(1), 244–252.

Rochira, F. & Thomas, C., 2023. On the importance of using directional information in the search for lower mantle reflectors, *Seismic Record,* **3**(2), 96–104.

Rost, S. & Thomas, C., 2009. Improving seismic resolution through array processing techniques, *Surv. Geophys.,* **30**(4–5), 271–299.

Saki, M., Wirp, S.A., Billen, M. & Thomas, C., 2024. Seismic evidence for possible entrainment of rising plumes by subducting slab induced flow in three subduction zones surrounding the Caribbean Plate, *Phys. Earth planet. Inter.,* **352,** 107212.

Shearer, P.M. & Masters, T.G., 1992. Global mapping of topography on the 660-km discontinuity, *Nature,* **335,** 791–796.

Stegman, D.R., 2003. *Thermochemical evolution of terrestrial planets: Earth, Mars, and the Moon, Ph.D.,* University of California, Berkeley, United States–California.

Stixrude, L. & Lithgow-Bertelloni, C., 2005. Thermodynamics of mantle minerals - I. Physical properties, *Geophys. J. Int.,* **162**(2), 610–632.

Stixrude, L. & Lithgow-Bertelloni, C., 2011. Thermodynamics of mantle minerals - II. Phase equilibria, *Geophys. J. Int.,* **184**(3), 1180–1213.

Stixrude, L. & Lithgow-Bertelloni, C., 2022. Thermal expansivity, heat capacity and bulk modulus of the mantle, *Geophys. J. Int.,* **228**(2), 1119–1149.

Tackley, P.J., 1993. Effects of strongly temperature-dependent viscosity on time-dependent, three-dimensional models of mantle convection, *Geophys. Res. Lett.,* **20**(20), 2187–2190.

Tackley, P.J & Xie, S., 2002. The thermochemical structure and evolution of Earth's mantle: constraints and numerical models, *Phil. Trans. R. Soc. A: Math. Phys. Eng. Sci.* **360,** 2593–2609.

Tauzin, B., Waszek, L., Ballmer, M.D., Afonso, J.C. & Bodin, T., 2022. Basaltic reservoirs in the Earth's mantle transition zone, *Proc. Natl Acad. Sci.,* **119**(48), e2209399119.

Thompson, D.A., Helffrich, G., Bastow, I.D., Kendall, J.M., Wookey, J., Eaton, D.W. & Snyder, D.B., 2011. Implications of a simple mantle transition zone beneath cratonic North America, *Earth planet. Sci. Lett.,* **312**(1–2), 28–36.

Van Heck, H.J., Davies, J.H., Elliott, T. & Porcelli, D., 2016. Global-scale modelling of melting and isotopic evolution of Earth's mantle: melting modules for TERRA, *Geosci. Model Develop.,* **9**(4), 1399–1411.

Verhoogen, J., 1965. Phase changes and convection in the Earth's mantle, *Phil. Trans. R. Soc. A: Math. Phys. Eng. Sci.,* **258**(1088), 276–283.

Walter, M.J., 2003. 2.08 Melt extraction and compositional variability in mantle lithosphere, in *Treatise on Geochemistry,* Eds. Holland,, H. D. & Turekian,, K. K., Vol. **2,** pp. 363–394, Elsevier.

Waszek, L., Schmerr, N.C. & Ballmer, M.D., 2018. Global observations of reflectors in the mid-mantle with implications for mantle structure and dynamics, *Nat. Commun.,* **9**(1), 1–13.

Waszek, L., Tauzin, B., Schmerr, N.C., Ballmer, M.D. & Afonso, J.C., 2021a. *Measurements of the 410 and 660 km discontinuities from global SS and PP precursors, ISC Seismological Dataset Repository*.

Waszek, L., Tauzin, B., Schmerr, N.C., Ballmer, M.D. & Afonso, J.C., 2021b. A poorly mixed mantle transition zone and its thermal state inferred from seismic waves, *Nat. Geosci.,* **14**(12), 949–955.

White, W. & Klein, E., 2014. Composition of the Oceanic Crust, in *Treatise on Geochemistry,* Vol. **4,** pp. 457–496, Elsevier.

Wieczorek, M.A. & Meschede, M., 2018. SHTools: Tools for Working with Spherical Harmonics, *Geochem. Geophys. Geosyst.,* **19**(8), 2574–2592.

Yan, J., Ballmer, M.D. & Tackley, P.J., 2020. The evolution and distribution of recycled oceanic crust in the Earth's mantle: insight from geodynamic models, *Earth planet. Sci. Lett.,* **537**.

Yu, C., Day, E.A., de Hoop, M.V., Campillo, M. & van der Hilst, R.D., 2017. Mapping mantle transition zone discontinuities beneath the Central Pacific with array processing of SS precursors, *J. geophys. Res.: Solid Earth,* **122**(12), 10364–10378.

Yu, Y., Gao, S.S. & Liu, K.H., 2020. Topography of the 410 and 660 km Discontinuities Beneath the Cenozoic Okavango Rift Zone and Adjacent Precambrian Provinces, *J. geophys. Res.: Solid Earth,* **125**(9).

Yu, Y.G., Wentzcovitch, R.M., Vinograd, V.L. & Angel, R.J., 2011. Thermodynamic properties of MgSiO3 majorite and phase transitions near 660 km depth in MgSiO3 and Mg2SiO 4: A first principles study, *J. geophys. Res.: Solid Earth,* **116**(2).

Zhao, L. & Chevrot, S., 2003. SS-wave sensitivity to upper mantle structure: implications for the mapping of transition zone discontinuity topographies, *Geophys. Res. Lett.,* **30**(11).